Journal of Materials Science & Technology 35 (2019) 2618–2624

Contents lists available at ScienceDirect

Journal of Materials Science & Technology

journal homepage: www.jmst.org

Letter

High-performance hot-warm rolled Zn-0.8Li alloy with nano-sized metastable precipitates and sub-micron grains for biodegradable stents

ARTICLE INFO

Keywords:
Zn-Li alloy
Mechanical properties
Three-dimensional atom probe
Precipitation
Recrystallization

ABSTRACT

Fabricated through a newly developed hot-warm rolling process, Zn-0.8Li (wt%) alloy has ideal strength and ductility far beyond the mechanical benchmark of materials for biodegradable stents. Precipitation of needle-like Zn in primary β-LiZn$_4$ phase is observed in Zn-Li alloy for the first time. Orientation relationship between them can be described as $[1\text{-}213]_\beta//[2\text{-}1\text{-}10]_{Zn}$, $(10\text{-}10)_\beta$ about 4.5° from $(0002)_{Zn}$. Zn grains with an average size of 640 nm exhibit strong basal texture, detected by transmission electron back-scatter diffraction. Li distribution is determined by three-dimensional atom probe, which reveals the formation of nano-sized metastable α-Li$_2$Zn$_3$ precipitates with a number density of 7.16×10^{22} m^{-3}. The fine lamellar Zn + β-LiZn$_4$ structure, sub-micron grains and the nano-sized precipitates contribute to the superior mechanical properties.

1. Introduction

Zinc (Zn) and its alloys have been investigated as biodegradable materials during the last decade. Previous reports have shown that they have good biocompatibility and moderate bio-corrosion rate [1–4]. However, Zn and its alloys fail to satisfy the clinical requirements for degradable intravascular stents in terms of mechanical properties (i.e., yield strength, YS > 200 MPa, ultimate tensile strength, UTS > 300 MPa and elongation, EL > 15%–18%), which hinders their clinical applications and further development [5].

Lithium (Li) is selected as an alloying element because of the possible hardening ability of the Zn+β-LiZn$_4$ eutectic structure, as shown in the Zn-Li binary phase diagram (Fig. 1(a)), which has been verified in Zn-0.4Li and Zn-0.7Li (wt%) alloy [6]. β-LiZn$_4$ has a close-packed hexagonal structure (HCP) with the lattice parameters of $a = 0.278$ nm and $c = 0.439$ nm [7], as illustrated in Fig. 1(b). Additionally, Li with a recommended intake of 0.1 mg for a 70 kg adult is an element to improve hematopoietic and immunological functions of a human body [8]. It has been reported that after implantation in the abdominal aorta of rats for 11 months, Zn-0.1Li alloy wire resulted in wide open arterial lumens and low neointimal growth, exhibiting excellent biocompatibility [9]. However, comprehensive mechanical properties of previously reported Zn-(0.1-0.8)Li alloys cannot satisfy the mechanical benchmark of materials for biodegradable stents. As-drawn Zn-0.1Li alloy exhibits UTS of only 274 MPa [9]. As-rolled Zn-(0.2-0.7)Li alloys exhibit elongation less than 15%, although their strengths are higher than the benchmark [6]. Hot-rolled Zn-0.8Li alloy with YS of 183.5 MPa and UTS of 238.1 MPa also fails to meet the benchmark [10]. Thus, improving the comprehensive mechanical properties of the Zn-Li alloys remains an urgent and challengeable task.

It is well understood that Li addition makes alloys more vulnerable to oxidation [11–13], which causes many difficulties for sample preparation and microstructure observation. Additionally, it is difficult to directly determine Li distribution in alloys due to the low characteristic radiation energy of Li. In various Li-containing alloys, Li distribution is mainly determined indirectly through crystal structures of Li-rich phases [14,15]. Probably due to these difficulties, three-dimensional Li distribution and grain orientation are still unknown for biodegradable Zn-Li alloys, making it challenging to establish the structure-properties relationships for these alloys.

In this work, a novel hot-warm rolling process is developed, which highly enhances the mechanical properties of the Zn-0.8Li alloy over the benchmark. Three-dimensional atom probe (3D-AP) and transmission electron back-scatter diffraction (T-EBSD) have been successfully employed to investigate the microstructure of Li-containing Zn alloys for the first time.

2. Experimental

2.1. Alloy preparation

High purity Zn (99.95 wt%) and Li (99.95 wt%) metals were used as raw materials to produce Zn-0.8Li alloy with 0.8 wt.% Li nominal composition. The raw materials were melted in a ZG-0.01 vacuum induction furnace under argon protection. The melt was kept at 500 °C for 40 min, and then poured into a graphite mold to obtain a cylinder ingot after natural cooling. The actual composition of the

https://doi.org/10.1016/j.jmst.2019.06.009
1005-0302/

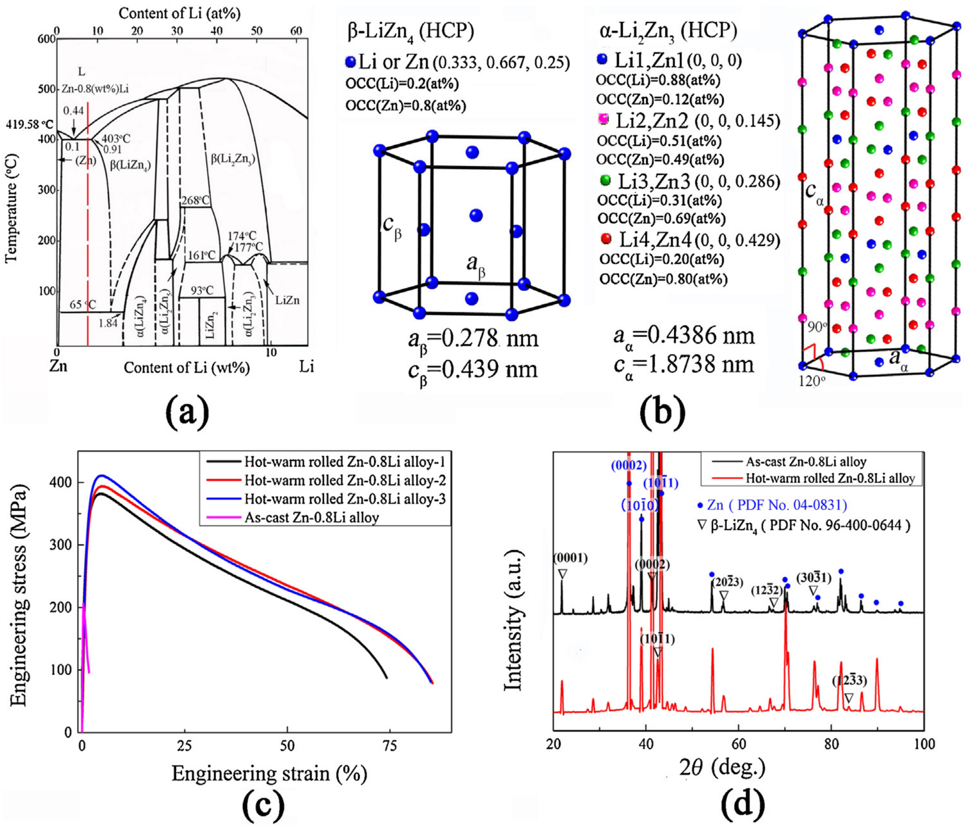

Fig. 1. (a) Zn-rich end of the Zn-Li binary phase diagram [22]. The red-dashed line indicates the composition of the Zn-0.8Li alloy; (b) crystal structures of β-$LiZn_4$ [7] and α-Li_2Zn_3 [23]. OCC refers to site occupation factor of an atom in a crystal structure; (c) engineering strain-stress curves of the as-cast and as-rolled Zn-0.8Li alloy; (d) XRD patterns of the as-cast and as-rolled Zn-0.8Li alloy.

alloy was measured to be Zn-0.75Li through inductively coupled plasma atomic emission spectrometry (ICP-AES), which is close to its 0.8 wt% Li nominal composition.

2.2. *Hot-warm rolling*

The ingots were first homogenized at 250 °C for 2 h and then at 350 °C for 2 h followed by furnace cooling. A newly developed hot-warm rolling process was applied to the homogenized alloy in order to eliminate its brittleness. First, the alloy was hot-rolled at 350 °C with a total thickness reduction of 75% by 4 passes and then quenched in cold water. Then, after annealing at 100 °C for 30 min, it was warm-rolled at 100 °C with a total thickness reduction of 60% by a single pass, followed by water quenching. The rolling, transverse and normal directions of the rolled plate are designated as RD, TD, and ND, respectively.

2.3. *Tensile testing and microstructure observation*

According to the ASTM E8, tensile specimens were machined from the hot-warm rolled (i.e., as-rolled) plates along RD. Tensile testing was performed using the Instron-5569 electronic universal testing machine with a strain rate of 3.3×10^{-4} s^{-1} at room temperature. At least three specimens were tested to obtain reliable results. The microstructure was examined using a transmission electron microscope (TEM, JEM-ARM200 F, JEOL, Japan) and a field emission scanning electron microscope (SEM, Auriga, Carl Zeiss, Germany) equipped with the Oxford NordlysNano EBSD camera. T-EBSD was used for mapping grains since their sizes could be several hundreds of nanometers after rolling. TEM and T-EBSD samples of 3 mm in diameter were prepared by twin-jet electro-polishing using a solution of 4% perchloric acid alcohol at -35 °C and 20 V. 3D-AP (LEAP-5000XR, Cameca, USA) was used to determine Li distribution in the alloy. A laser pulse mode with a green laser of 60 pJ energy and 200 kHz frequency was used. 3D-AP specimens were prepared in an SEM with the focused-ion beam (SEM/FIB, Helios Nanolab 600i, FEI, USA). Phases were also checked by X-ray diffraction (XRD, Rigaku D-max/2500 PC, Japan) with Cu Kα radiation and a scanning speed of 2°/min.

Table 1
Mechanical properties of the Zn-0.8Li alloy.

State	YS (MPa)	UTS (MPa)	EL (%)
As-cast	194.6 ± 20.7	213.7 ± 33.7	0.2 ± 0.1
As-rolled	261.5 ± 40.8	401.4 ± 51.6	80.8 ± 9.7
Clinical requirements for mechanical benchmark [5]	200	300	15-18

3. Results and discussion

3.1. *Mechanical properties*

Tensile mechanical properties of the Zn-0.8Li alloy in the as-cast and as-rolled states are listed in Table 1. Representative engineering strain-stress curves are given in Fig. 1(c). YS, UTS, and EL of the as-cast alloy are 194.6 MPa, 213.7 MPa, and 0.2%, respectively, which fail to meet the benchmark for the clinical requirements. Both the strength and the ductility of the alloy are significantly enhanced after hot-warm rolling. Compared to the as-cast state, YS and UTS of the as-rolled alloy increase to 261.5 MPa and 401.4 MPa, respectively. Moreover, the hot-warm rolling induces a significant brittle-to-ductile transition. The EL of the as-rolled alloy skyrockets

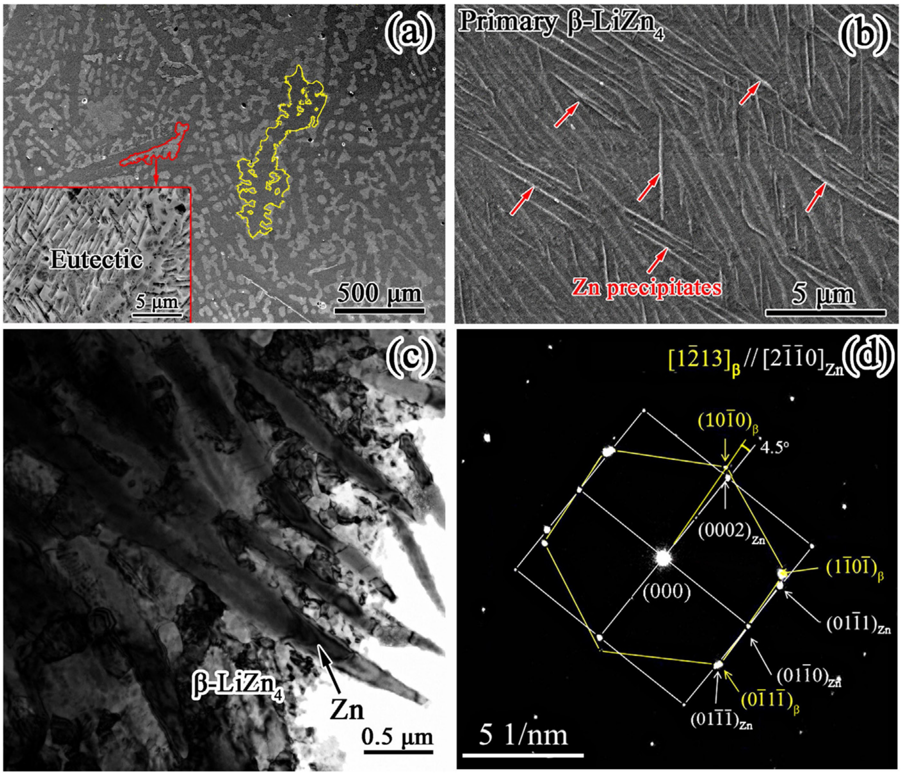

Fig. 2. (a) Morphology of the as-cast alloy consisting of coarse primary β-LiZn$_4$ dendrites and Zn+β-LiZn$_4$ eutectics; (b) enlarged view of the yellow solid line marked region in (a), showing needle-like Zn precipitates in the primary β-LiZn$_4$ phase; (c) TEM bright field (BF) image of the Zn precipitates; (d) Overlapped diffraction patterns of Zn precipitates and β-LiZn$_4$ matrix along $[2\text{-}1\text{-}10]_{Zn}//[1\text{-}213]_\beta$ zone axis.

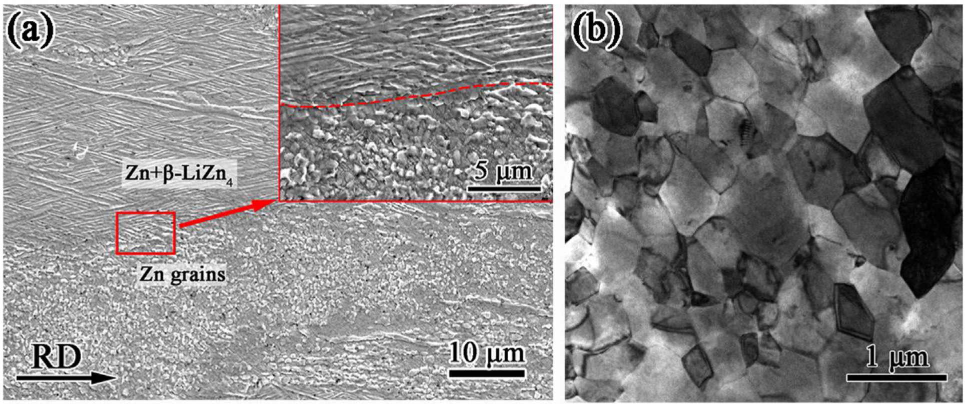

Fig. 3. (a) SEM image of the as-rolled alloy and (b) TEM BF image of Zn grains in as-rolled alloy.

to 80.8%. Therefore, YS, UTS, and EL of the as-rolled alloy are 30.5%, 33.3% and 403% higher than the benchmark, respectively, indicating that biodegradable stents made from this material can provide reliable mechanical support.

As shown in Fig. 1(c), the engineering stress of the as-rolled Zn-0.8Li alloy declines after the UTS. Similar work softening phenomenon also appears in other biodegradable Zn alloys [16–18]. The maximum strain during stent expansion and the radial force of a stent depend on its design, diameter, thickness and so on [19,20]. For instance, the maximum value of the nominal strain in the CYPHER^{TM} coronary stent is estimated to be 23% [21], which corresponds to engineering stresses over 300 MPa of the as-rolled Zn-0.8Li alloy. Therefore, Zn-0.8Li alloy are likely to provide enough mechanical support for expanded stents in clinical application.

3.2. *Microstructure of Zn-0.8Li alloy*

XRD patterns in Fig. 1(d) show that Zn-0.8Li alloy either in the as-cast or in the as-rolled status contains Zn and β-LiZn$_4$ phases, both of which have also been found in Zn-0.7Li alloy [6]. According to Zn-Li binary phase diagram, decomposition of β-LiZn$_4$ into Zn and α-LiZn$_4$ happens at 65 °C during cooling in thermodynamic equilibrium condition. No α-LiZn$_4$ phase is detected in the as-cast alloy probably due to a cooling rate much faster than that in the equilibrium condition. The warm rolling temperature of 100 °C is 35 °C higher than the decomposition temperature. After the warm rolling, the plates are water quenched, which freezes β-LiZn$_4$ down to room temperature.

SEM image of the as-cast alloy is shown in Fig. 2(a), in which it can be seen clearly that the microstructure consists of darker

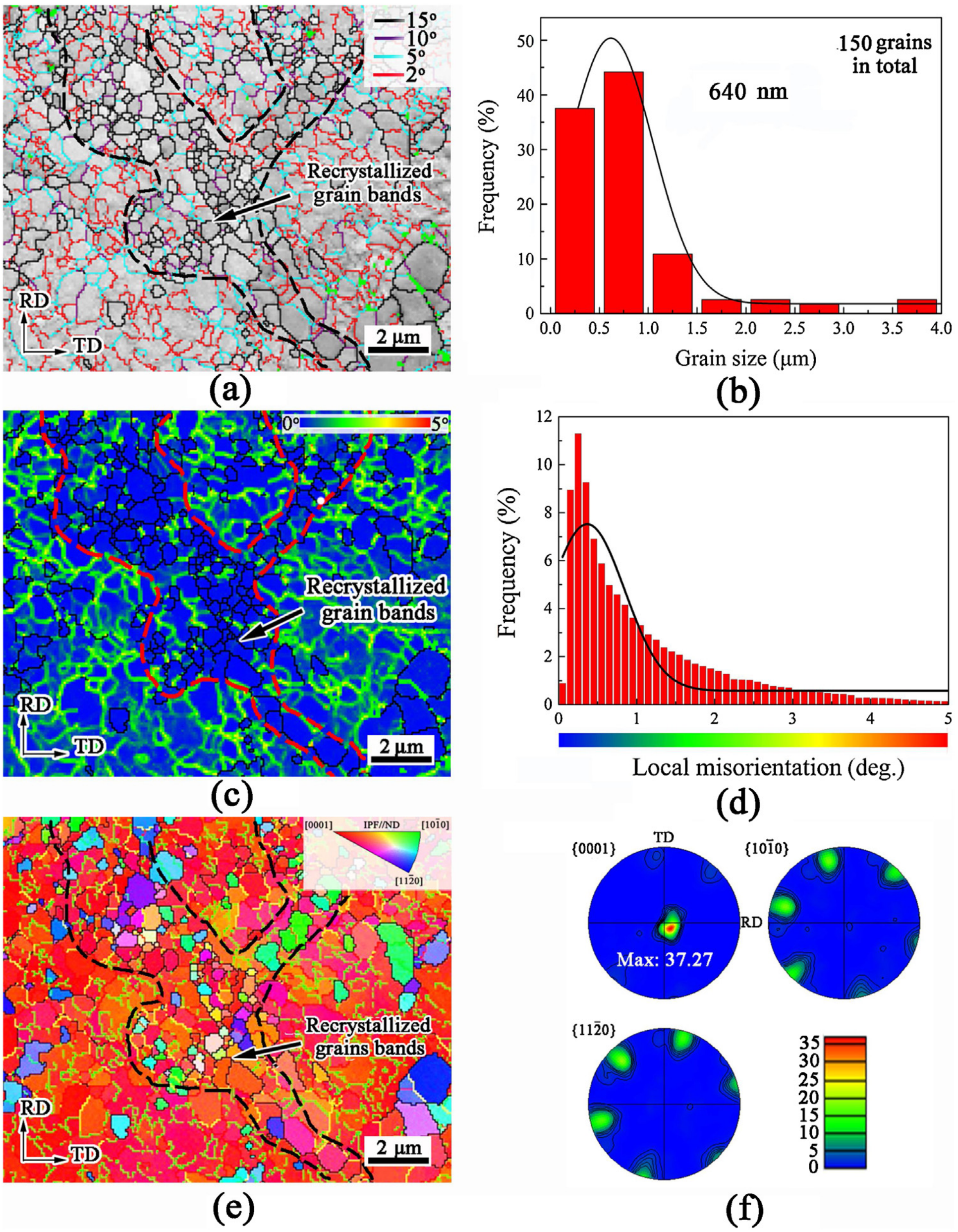

Fig. 4. T-EBSD measured microstructure of the as-rolled alloy: (a) band contrast map clearly showing large-angle grain boundaries, low-angle grain boundaries and subgrain boundaries; (b) statistical analysis of the grain sizes; (c) Kernel average misorientation (KAM) map with the color bar corresponding to the local misorientations in (c) ranging from 0° to 5°; (d) statistical analysis of local misorientations corresponding to (c); (e) the microstructure colored according to the inverse pole figure (IPF) parallel to ND; (f) {0001}, {10-10} and {11-20} pole figures.

and brighter regions. The area fraction of the darker region reaches 67.7%. According to Zn-Li binary phase diagram, primary β-$LiZn_4$ phase first forms during solidification. Based on the lever rule, it can be calculated that the volume fraction of primary β-$LiZn_4$ phase with a theoretical density of 6.73 g/cm^3 is 67.2% at the eutectic temperature of 403 °C. The calculated volume fraction is close to the measured area fraction, so that the darker region in Fig. 2(a) should be primary β-$LiZn_4$ phase, which consists of coarse dendrites due to crystal growth in alloy melt, a common phenomenon observed in various alloys. The β-$LiZn_4$ dendrites have an average primary arm length of 916 ± 242 µm.

According to Zn-Li binary phase diagram, Zn+β-$LiZn_4$ eutectics should form among the primary β-$LiZn_4$ dendrites, which are confirmed in Fig. 2(a). An enlarged view of the brighter region in Fig. 2(a) in the inserted figure reveals that it has a lamellar structure, typical for eutectics. The lengths of the eutectics range from 30 µm to 100 µm. It should also be noted in Fig. 2(a) that the darker region is lower than the brighter region after etching. Standard electrode potentials (E°) of Li (i.e. -3.04 V) is much lower than that of Zn (i.e., -0.76 V). It can be seen in Fig. 1(b) that the crystal structure of β-$LiZn_4$ resembles a solid solution of Li in Zn crystal. The substitution of Zn atoms with Li atoms will make E° of Zn more negative, so that β-$LiZn_4$ corrodes faster than Zn due to galvanic corrosion. Since Li is difficult to be directly detected in such a low amount in the alloy, the characteristic topography is helpful to differentiate β-$LiZn_4$ from Zn.

According to Fig. 1(a), during cooling, Zn contents in β-$LiZn_4$ decreases considerably, which will result in the precipitation of Zn. This is confirmed in Fig. 2(b), in which dense needle-like Zn precipitates form in β-$LiZn_4$ matrix. Consistently, the Zn precipitates in a brighter contrast are higher than the β-$LiZn_4$ matrix due to the aforementioned electrochemical corrosion effect. Overlapped

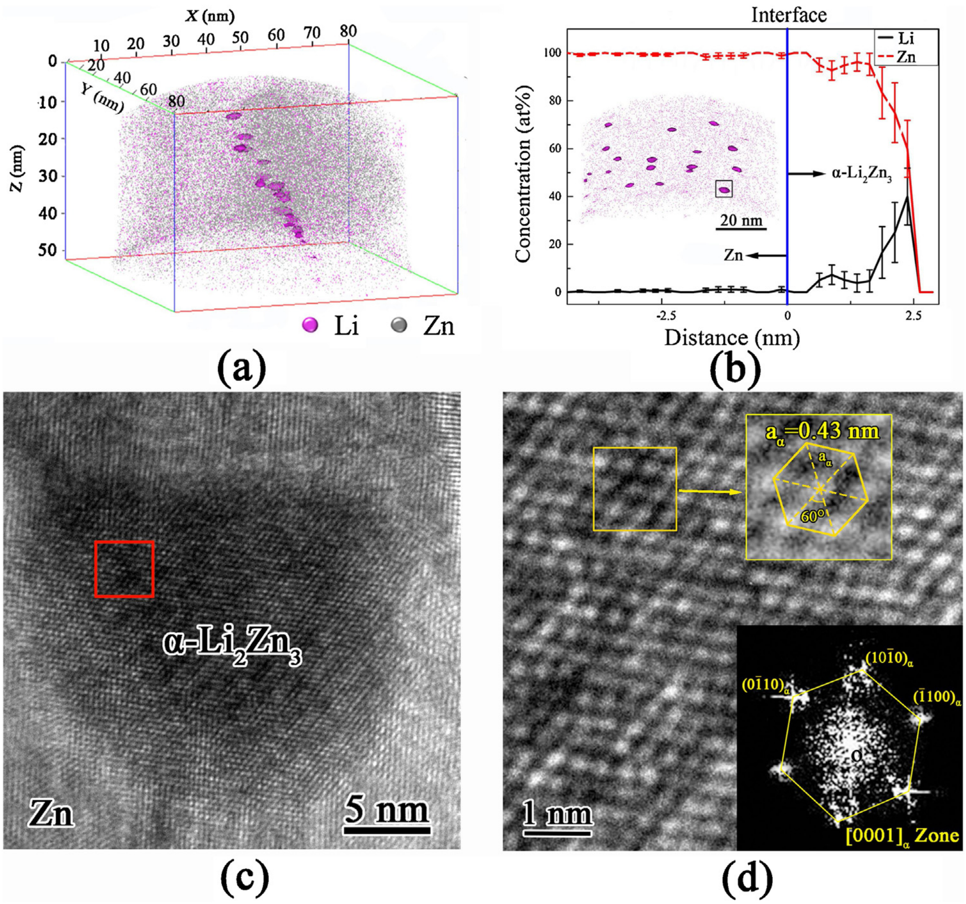

Fig. 5. (a) Distribution of Li atoms in the as-rolled alloy measured by 3D-AP, in which an isoconcentration surface encompasses regions containing more than 0.1 at.% Li; (b) proximity histogram of a representative nano-sized α-Li_2Zn_3 precipitates encompassed by a black open square; (c) HRTEM image of the α-Li_2Zn_3 precipitate; (d) FFT filtered micrograph of the red square marked region in (c) with an inset of its corresponding FFT patterns indexed. The yellow squared region is enlarged to show the crystal structure viewed from the $[0001]_α$ zone axis more clearly.

diffraction patterns of a Zn precipitate in Fig. 2(c) is given in Fig. 2(d). The β-$LiZn_4$ (HCP, a=b = 0.2782 nm, c = 0.4385 nm) matrix is oriented along $[1\text{-}213]_β$ zone axis, while the Zn (HCP, a=b = 0.2665 nm, c = 0.4947 nm) [24] precipitate is oriented along $[2\text{-}1\text{-}10]_{Zn}$ zone axis. It can be measured in Fig. 2(d) that $(10\text{-}10)_β$ deviates about 4.5° anticlockwise from $(0002)_{Zn}$, so that the orientation relationship (OR) can be described as $[1\text{-}213]_β//[2\text{-}1\text{-}10]_{Zn}$, $(10\text{-}10)_β$ about 4.5° from $(0002)_{Zn}$, which is reported for the first time as far as our knowledge.

The as-rolled alloy is composed of fine-grained Zn phase and elongated β-$LiZn_4$ bands with needle-like Zn precipitates, as shown in Fig. 3(a). The average width between two needle-like Zn precipitates is 0.44 ± 0.06 μm, about 35% less than that in the as-cast alloy. As can be seen in the insert figure in Fig. 3(a), Zn grains are fine, with an average size ranged from 0.3 μm to 0.7 μm, which is confirmed by TEM characterization in Fig. 3(b). The hot-warm rolling significantly refines Zn grains and changes the coarse primary β-$LiZn_4$ dendrites into elongated bands, resulting in the dramatic increase in both the strength and the ductility.

3.3. T-EBSD analysis of recrystallized Zn grains in as-rolled alloy

A representative microstructure measured by the T-EBSD is shown in Fig. 4(a). Grain boundaries (GBs) are outlined according to crystal misorientations. Large-angle GBs with misorientations larger than 15° are outlined in black. Low-angle GBs with 5-15° misorientations and sub-GBs with 2°-5° misorientations are outlined in purple (> 10°), blue (> 5°) and red (> 2°), respectively. In a branched band outlined by dashed lines, 87 Zn grains are enclosed by large-angle GBs, the size of which (i.e. equivalent diameter) is calculated to be 530 ± 230 nm. Taking aspect ratios $\leq$ 2 as a criterion [25], most of them are equiaxed grains. However, in the regions outside the band, few grains can be completely enclosed by large-angle GBs. The grains in these regions are divided by low-angle GBs and sub-GBs. The branched band consists of recrystallized Zn grains, while outside the band Zn grains have not been recrystallized. There are 150 grains enclosed by the large-angle GBs in total in Fig. 4(a), and their average size is 640 ± 440 nm (Fig. 4(b)). Large non-recrystallized grains outside the band can reach the size of about 4 μm. The kernel average misorientation map in Fig. 4(c) shows that the grains in the band have very small local misorientations of less than 1° (Fig. 4(d)). However, outside the band, much higher misorientation is in the vicinity of low-angle and sub-GBs. It is further confirmed that the branched band in Fig. 4(a) is composed of recrystallized Zn grains. In order to show grain orientation, the same region in Fig. 4(a) is shown in Fig. 4(e), colored according to the inverse pole figure. Most of the region is in red, indicating that most grains' c-axes (i.e., [0001]) are nearly parallel to ND. The pole figure in Fig. 4(e) confirms that Zn grains exhibit a strong basal texture. However, in the recrystallized grain band, many grains are green or blue, colors close to [11-20] and [10-10] corners of the inverse pole figure (IPF), indicating that the basal texture is weakened in this band.

Dynamic recrystallization easily occurs in Zn because of its low stacking fault energy [26]. The recrystallization temperatures of various Zn alloys range from 73 °C to 143 °C [27]. It was reported that the average grain size in Zn-0.8Li alloy after hot rolling at 250 °C is 5 μm [10], which is almost 9 times larger than that in the hot-warm rolled Zn-0.8Li alloy. According to the Hall-Patch relationship [28], the significant grain refinement contributes to the much higher mechanical properties of the hot-warm rolled Zn-0.8Li alloy. Warm rolling at 100 °C results in incomplete dynamic recrystallization and avoids abnormal grain growth. Then, water quenching after the warm rolling hinders further growth of recrystallized grains. Thus, warm rolling and water quenching facilitate the formation of the fine grain microstructure. Moreover, sub-micro grains in the as-rolled alloy can alleviate stress concentration by spreading the stress, which avoids crack propagation effectively and increases the ductility of the as-rolled alloy dramatically [29].

3.4. 3D-AP and HRTEM analysis of α-Li_2Zn_3 phase in the as-rolled alloy

Three-dimensional Li distribution has been determined directly in the Zn alloy by the 3D-AP for the first time (Fig. 5(a)). There are Li-rich regions in the Li-depleted Zn matrix. The concentration of Li in the Li-depleted Zn matrix is calculated to fluctuate around 0.1 at.%, i.e., equivalent to 0.01 wt%, agreeing well with the Zn-Li binary phase diagram at lower temperatures. Therefore, 0.1 at% Li is chosen to be a criterion for drawing the isoconcentration surface. Within a volume of 2.5×10^{-22} m^{-3} after three-dimensional reconstruction in Fig. 5(a), eighteen Li-enriched elliptic precipitates are highlighted by the isoconcentration surface of 0.1 at.% Li, with a number density of 7.16×10^{22} m^{-3}. Their long axes range from 2.6 nm to 6 nm, with an average value of 4.4 ± 0.8 nm. Representative proximity histogram is shown in Fig. 5(b). The atomic ratio of Li to Zn in its core region is calculated to be 2/3, in agreement with the α-Li_2Zn_3 phase in the Zn-Li binary phase diagram (Fig. 1(a)). Clearly, this is a metastable phase, since the equilibrium phase constitution should be Zn+β-$LiZn_4$. Moreover, statistical analysis of the eighteen precipitates confirms that the Li to Zn ratio is around 2/3. HRTEM observations further confirm the existence of metastable α-Li_2Zn_3 precipitates. One with a diameter of 9.4 nm is shown in Fig. 5(c), and the region enclosed by the red solid lines is enlarged in Fig. 5(d). The periodic lattice distribution projected along the $[0001]_\alpha$ zone axis (see the inset in Fig. 5(d)) agrees well with the crystal structure of the α-Li_2Zn_3 phase (Fig. 1(b)).

In the Zn-(0.1-0.7)Li alloys, no Li-rich precipitates have been reported yet [6,9]. In the hot-rolled Zn-0.8Li alloy, globular β-$LiZn_4$ precipitates are detected, typically with average diameter of 24 nm [10], which are almost 5 times larger than the metastable α-Li_2Zn_3 precipitates. This difference is mainly attributed to the novel hot-warm rolling process. The water quenching after hot rolling results in the Zn matrix supersaturated with Li solute, which creates thermodynamic conditions for precipitation during the following warm rolling. Consequently, metastable α-Li_2Zn_3 precipitates with very fine sizes and high number density can significantly strengthen the alloy due to the pinning effect.

4. Conclusions

In summary, a novel hot-warm rolling process has been successfully demonstrated for fabricating Zn-0.8Li alloy with superior strength and ductility simultaneously. The superior mechanical properties are attributed to the fine lamellar Zn+β-$LiZn_4$ structure, sub-micron grains and metastable α-Li_2Zn_3 precipitate. The brief conclusions can be drawn:

(1) Dense needle-like Zn precipitates form in primary β-$LiZn_4$ phase, the OR between β-$LiZn_4$ matrix and Zn precipitates can be described as $[1\text{-}213]_\beta//[2\text{-}1\text{-}10]_{Zn}$, $(10\text{-}10)_\beta$ about 4.5° from $(0002)_{Zn}$.
(2) The sub-micron grains are characterized through the T-EBSD analysis, which have an average size of 530 nm and form a recrystallized grain band.
(3) The high-density metastable α-Li_2Zn_3 precipitates are revealed through combined analysis of 3D-AP and HRTEM, which are ellipsoid-shaped with an average size of 4.4 nm.

Therefore, the hot-warm rolled Zn-0.8Li alloy can provide sufficient mechanical supporting as biomedical materials.

Acknowledgements

This work was supported financially by the National Key R&D Program of China (No. 2016YFC1102500) and the National Natural Science Foundation of China (No. 51871020).

References

[1] J. Venezuela, M.S. Dargusch, Acta Biomater. 87 (2019) 1–40.
[2] L. Liu, Y. Meng, C. Dong, Y. Yan, A.A. Volinsky, L. Wang, J. Mater. Sci. Technol. 34 (2018) 2271–2282.
[3] C. Xiao, L. Wang, Y. Ren, S. Sun, E. Zhang, C. Yan, J. Mater. Sci. Technol. 34 (2018) 1618–1627.
[4] C. Wang, H. Yang, X. Li, Y. Zheng, J. Mater. Sci. Technol. 32 (2016) 909–918.
[5] P.K. Bowen, J. Drelich, J. Goldman, Acta Biomater. 25 (2013) 2577–2582.
[6] S. Zhao, C.T. McNamara, P.K. Bowen, N. Verhun, J.P. Braykovich, J. Goldman, J.W. Drelich, Metall. Mater. Trans. A 48 (2017) 1204–1215.
[7] M.P. Bichat, J.L. Pascal, F. Gillot, F. Favier, J. Phys. Chem. Solids 67 (2006) 1233–1237.
[8] W. Young, Cell Transplant. 18 (2009) 951–975.
[9] S. Zhao, J. Seitz, R. Eifler, H.J. Maier, R.J. Guillory, E.J. Earley, A. Drelich, J. Goldman, J.W. Drelich, Mater. Sci. Eng. C 76 (2017) 301–312.
[10] Y. Zhang, Y. Yan, X. Xu, Y. Lu, L. Chen, D. Li, Y. Dai, Y. Kang, K. Yu, Mater. Sci. Eng. C 99 (2019) 1021–1034.
[11] C. Li, D. Xu, X. Chen, B. Wang, R. Wu, E. Han, N. Birbilis, Electrochim. Acta 260 (2018) 55–64.
[12] Z. Ding, L. Cui, R. Zeng, Y. Zhao, S. Guan, D. Xu, C. Lin, J. Mater. Sci. Technol. 34 (2018) 1550–1557.
[13] N. Ott, Y. Yan, S. Ramamurthy, S. Kairy, N. Birbilis, Scr. Mater. 119 (2016) 17–20.
[14] C. Li, D. Xu, S. Yu, L. Sheng, E. Han, J. Mater. Sci. Technol. 33 (2017) 475–480.
[15] Z. Zhao, X. Xing, J. Ma, L. Bian, W. Liang, Y. Wang, J. Mater. Sci. Technol. 34 (2018) 1564–1569.
[16] E. Mostaed, M.S. Ardakani, M. Sikora-Jasinska, J.W. Drelich, Mater. Lett. 244 (2019) 203–206.
[17] Z. Shi, J. Yu, X. Liu, L. Wang, J. Mater. Sci. Technol. 34 (2018) 1008–1015.
[18] Z. Tang, J. Niu, H. Huang, H. Zhang, J. Peia, J. Oub, G. Yuan, J. Mech. Behav. Biomed. Mater. 72 (2017) 182–191.
[19] M. Azaouzi, A. Makradi, S. Belouettar, Comput. Mater. Sci. 72 (2013) 54–61.
[20] T. Matsumoto, Y. Matsubara, Y. Aoyagi, D. Matsuda, J. Okadome, K. Morisaki, K. Inoue, S. Tanaka, T. Ohkusa, Y. Maehara, Vascular 1 (2015) 1–6.
[21] M. De Beule, P. Mortier, J. Belis, R. Van Impe, B. Verhegghe, P. Verdonck, Key Eng. Mater. 340–341 (2007) 841–846.
[22] A.D. Pelton, J. Phase Equilibria 12 (1991) 42–45.
[23] V.V. Pavlyuk, I.V. Chumak, H. Ehrenberg, Acta Cryst. B 68 (2012) 34–39.
[24] T.B. Massalski, H.W. King, Acta Metall. 10 (1962) 1171–1181.
[25] Z. Shi, J. Yu, X. Liu, Mater. Des. 144 (2018) 343–352.
[26] M.E. Kassner, S.R. Barrabes, Mater. Sci. Eng. A 410–411 (2005) 152–155.
[27] A.K. Bhargava, C.P. Sharma, Mechanical Behavior and Testing of Materials, PHI Learning, 2012.
[28] M. Sokol, M. Halabi, Y. Mordekovitz, S. Kalabukhov, S. Hayun, N. Frage, Scr. Mater. 139 (2017) 159–161.
[29] J.A. del Valle, F. Carren, O.A. Ruano, Acta Mater. 54 (2006) 4247–4259.

Zhen Li
Beijing Advanced Innovation Center for Materials Genome Engineering, State Key Laboratory for Advanced Metals and Materials, School of Materials Science and Engineering, University of Science and Technology Beijing, Beijing, 100083, China

Zhang-Zhi Shi*
Beijing Laboratory of Metallic Materials and Processing for Modern Transportation, School of Materials Science and Engineering, University of

Science and Technology Beijing, Beijing, 100083, China

Yuan Hao
Hua-Fang Li
Beijing Advanced Innovation Center for Materials Genome Engineering, State Key Laboratory for Advanced Metals and Materials, School of Materials Science and Engineering, University of Science and Technology Beijing, Beijing, 100083, China

Xue-Feng Liu
Beijing Laboratory of Metallic Materials and Processing for Modern Transportation, School of Materials Science and Engineering, University of Science and Technology Beijing, Beijing, 100083, China

Alex A. Volinsky
Department of Mechanical Engineering, University of South Florida, Tampa, FL, 33620, USA

Hai-Jun Zhang[a,b]
[a] *Department of Interventional and Vascular Surgery, The Tenth People's Hospital of Shanghai, Tongji University, Shanghai, 200072, China*
[b] *National United Engineering Laboratory for Biomedical Material Modification, Branden Industrial Park, Qihe Economic & Development Zone, Dezhou, 251100, China*

Lu-Ning Wang**
Beijing Advanced Innovation Center for Materials Genome Engineering, State Key Laboratory for Advanced Metals and Materials, School of Materials Science and Engineering, University of Science and Technology Beijing, Beijing, 100083, China

* Corresponding author.

** Corresponding author.
E-mail addresses: ryansterne@163.com (Z.-Z. Shi), luning.wang@ustb.edu.cn (L.-N. Wang).

11 April 2019